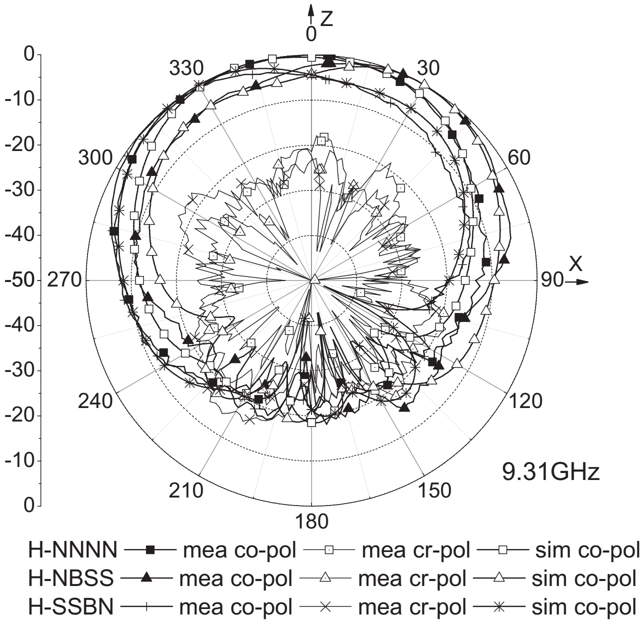

(*a*)H mode

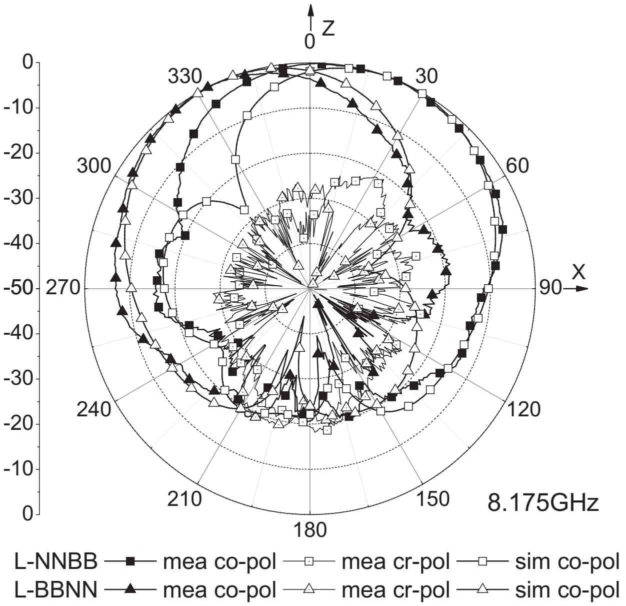

(*b*) L mode

**Figure 4** Measured and simulated radiation patterns in the *E*-plane of the antenna. (a) H-mode. (b) L-mode

operating at two different frequencies, 8.175 and 9.31 GHz. The radiation pattern reconfiguration is achieved by using switched slots on the parasitic element patches. By changing the states of the parasitic element patches, the antenna can change the directions of the radiation beams. At the two operating frequencies, the coverage of radiation pattern of the antenna is similar. At the higher frequency of 9.31 GHz, continuous radiation coverage from −71° to +61° in the *E*-plane can be obtained by using three radiation modes. At the lower frequency of 8.175 GHz, continuous radiation coverage from −56° to +56° in the *E*-plane can be obtained by using two radiation modes. With the rapid development of switches, the effect of the switches on the design of the antenna has been reduced a lot and will be even clear out. Thus, while in this article real switches are not utilized, the characteristics in frequency and pattern reconfiguration of the antenna are well demonstrated.

## ACKNOWLEDGMENTS

This work was supported in part by the National Natural Science Foundation of China and The Youth Foundation of UESTC. The authors acknowledge Dr. Long Jin and Mr. Shi-Wei Qu for their assistance.

## REFERENCES

1. S. Xiao, B.-Z. Wang, and X.-S. Yang, A novel frequency-reconfigurable patch antenna, Microwave Opt Technol Lett 36 (2003), 295-297.
2. P.F. Wahid, M.A. Ali, and B.C. DeLoach Jr., A reconfigurable Yagi antenna for wireless communications, Microwave Opt Technol Lett 38 (2003), 140-141.
3. S. Zhang, G.H. Huff, J. Feng, and J.T. Bernhard, A pattern reconfigurable microstrip parasitic array, IEEE Trans Antennas Propag 52 (2004), 2773-2776.
4. G.H. Huff and J.T. Bernhard, Integration of packaged RF MEMS switches with radiation pattern reconfigurable square spiral microstrip antennas, IEEE Trans Antennas Propag 54 (2006), 464-469.
5. S. Nikolaou, R. Bairavasubramanian, C. Lugo, D.C. Thompson, and G.E. Ponchak, Pattern and frequency reconfigurable annular slot antenna using PIN diodes, IEEE Trans Antennas Propag 54 (2006), 439-448.
6. C.J. Panagamuwa, A. Chauraya, and J.C. Vardaxoglou, Frequency and beam reconfigurable antenna using photoconducting switches, IEEE Trans Antennas Propag 54 (2006), 449-454.
7. X.-S. Yang, B.-Z. Wang, W. Wu, and S. Xiao, Yagi patch antenna with dual-band and pattern reconfigurable characteristics, IEEE Antennas Wireless Propag Lett 6 (2007), 168-171.
8. J. Huang and A.C. Densmore, Microstrip Yagi array antenna for mobile satellite vehicle application, IEEE Trans Antennas Propag 39 (1991), 1024-1030.

---

# INFRARED PHASED-ARRAY ANTENNA

**Christopher T. Middlebrook,[1] Peter M. Krenz,[1] Brian A. Lail,[2] and Glenn D. Boreman[1]**
[1] College of Optics and Photonics/CREOL, University of Central Florida, Orlando, FL 32816; Corresponding author: pkrenz@creol.ucf.edu
[2] Electrical and Computer Engineering, Florida Institute of Technology, Melbourne FL, 32901

*Received 19 July 2007*

**ABSTRACT:** *Phased addition of currents from multiple dipole antennas is demonstrated for the first time at a wavelength of 10.6 μm. Coplanar strip lines are used to interconnect the antennas, preserving the phase of the individual infrared-frequency currents, which are summed together at a common bolometric load. Angular pattern measurements on two-element dipole arrays show that the direction of maximum response depends on the phase difference between the currents contributed from each antenna, evaluated at the bolometer location. As more antennas are added together in phase, beam narrowing is observed.* © 2008 Wiley Periodicals, Inc. Microwave Opt Technol Lett 50: 719–723,

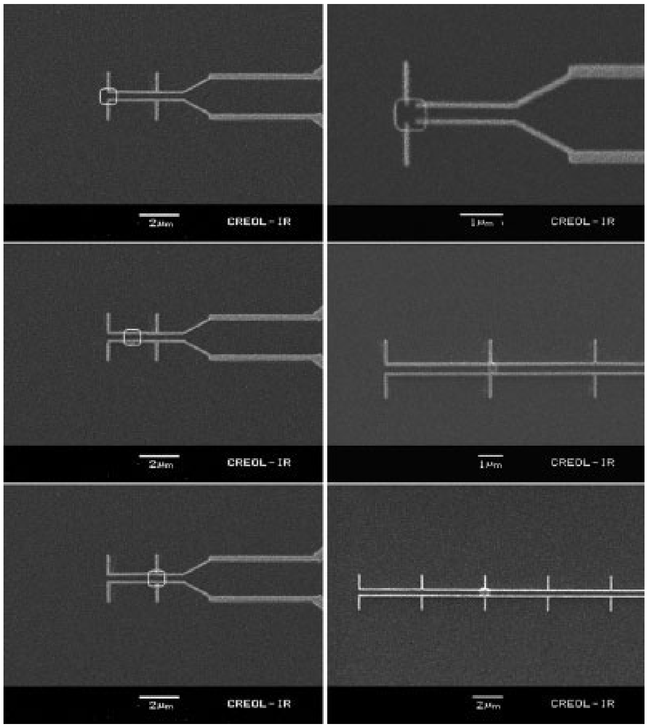

**Figure 1** Left column: (top) dual-dipole antenna with bolometer left, (center) dual-dipole antenna with bolometer centered, and (bottom) dual-dipole antenna with bolometer right; Right column: (top) single element, (center) three-element array, (bottom) five-element array

2008; Published online in Wiley InterScience (www.interscience.wiley.com). DOI 10.1002/mop.23213

**Key words:** *antenna-coupled detector; phased array; infrared antenna*

## 1. INTRODUCTION

Antenna phasing concepts are demonstrated at infrared wavelengths. The phase relationship between induced currents from multiple antennas determines the angular response, allowing beam scanning and shaping. Infrared-frequency coplanar strip (CPS) lines are used to interconnect the antennas, preserving phase information. For two lithographic dipole antennas, the phase with which the currents add at the load is determined by the location of the bolometer along the CPS line that joins the antennas. The direction of maximum antenna response depends on the load position. Next, we compare the angular pattern of a single-element dipole to measurements of three- and five-element arrays. The arrays with additional antennas have narrower patterns. Figure 1 shows the devices measured.

## 2. DEVICES CHARACTERIZED

Infrared dipole-antenna arrays were fabricated on the flat side of a silicon immersion lens, at the center of curvature of the lens surface [1]. The antennas were illuminated through the curved surface, allowing us to exploit the preferential response of antennas on a dielectric substrate to radiation from the high-permittivity side [2], while avoiding generation of substrate modes and distortion of the angular pattern by refraction effects [3]. The dipole length of 2.4 $\mu$m was designed to approximate a half-wave resonance, considering that the air/Si boundary has an effective refractive index (square root of mean permittivity) of about 2.5. We use previous characterizations of these CPS lines, the results of which were the propagation constant $\beta = 1.48$ radians/$\mu$m, and attenuation of 0.10 Np/$\mu$m [4]. The spacing between antennas in the two-dipole array was chosen to be 2.4 $\mu$m, resulting in an interelement phase difference of about 200° for current waves generated by the two dipoles. For the three- and five-element arrays, the dipoles were spaced by 4.2 $\mu$m, yielding an interelement phase difference of about 360°, in order to produce a broadside maximum in the response.

## 3. THEORETICAL PATTERNS

Pattern multiplication was used to calculate the array patterns as the product of the single-element pattern and the array factor. The H-plane array factor was determined using standard techniques [5]. We previously developed an expression for the H-plane substrate-side pattern for a single dipole at an air/Si interface [3]. Squaring the resulting products yielded Eqs. (1) and (2), the theoretical H-plane substrate-side power patterns.

$$S_{\text{Total}} = [(1 + a\cos\psi)^2 + (a\sin\psi)^2] \times \frac{n_{\text{air}}}{2}\left|\frac{2\cos\theta}{\cos\theta + \dfrac{n_{\text{air}}}{n_{\text{Si}}}\cos\theta}\right|^2 \times \left|\frac{2\cos\theta}{\cos\theta + \dfrac{n_{\text{Si}}}{n_{\text{air}}}\cos\theta}\right|^2 \left|\frac{2\cos\theta}{\cos\theta + \dfrac{n_{\text{air}}}{n_{\text{si}}}\cos\left(\sin^{-1}\left(\dfrac{\sin\theta}{n_{\text{si}}}\right)\right)}\right|^2 \quad (1)$$

In Eq. (1), $a$ is the relative difference in amplitudes between the two dipoles, $\theta$ is the incident angle, and $\psi = \phi\cos(\theta) + \alpha$,

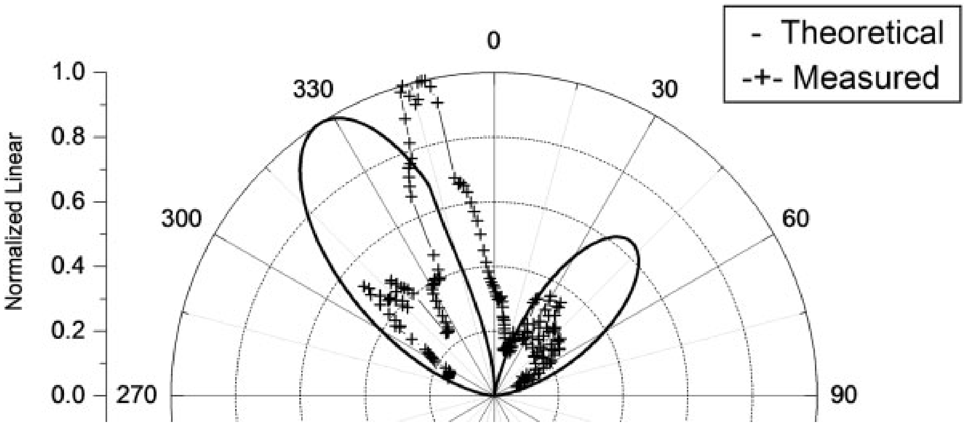

**Figure 2** H-plane substrate-side power pattern for dual-dipole antenna array with bolometer shifted to the right

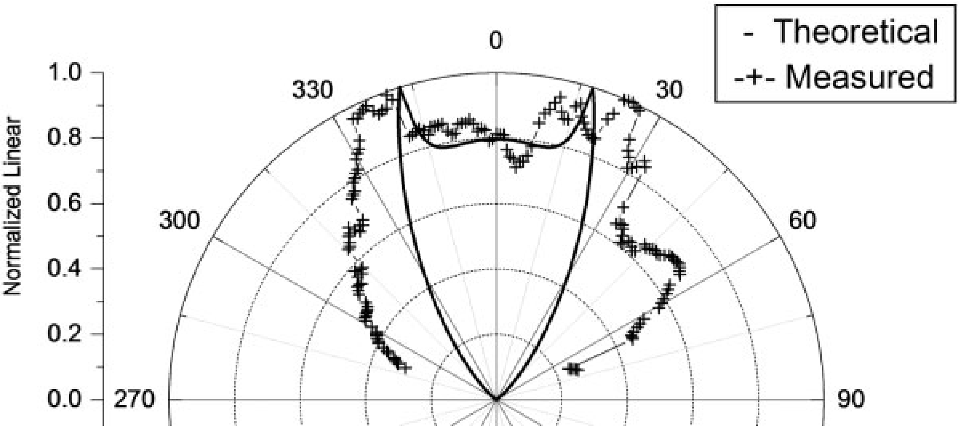

**Figure 3** H-plane substrate-side power pattern for dual-dipole antenna array with bolometer centered

where $\alpha$ is determined by the bolometer location with respect to the dipoles. The phase shift $\phi = \beta d = (2\pi/\lambda_{\text{eff}})d$ depends on the CPS line length ($d$).

$$S_T = \{a_1 + a_2 \cos[\beta d \cos\theta + \alpha] + a_3 \cos[2\beta d \cos\theta + \alpha]\}^2 \times \frac{n_{\text{air}}}{2}\left|\frac{2\cos\theta}{\cos\theta + \frac{n_{\text{air}}}{n_{\text{Si}}}\cos\theta}\right|^2 \times \left|\frac{2\cos\theta}{\cos\theta + \frac{n_{\text{Si}}}{n_{\text{air}}}\cos\theta}\right|^2 \left|\frac{2\cos\theta}{\cos\theta + \frac{n_{\text{air}}}{n_{\text{si}}}\cos\left(\sin^{-1}\left(\frac{\sin\theta}{n_{\text{si}}}\right)\right)}\right|^2 \qquad (2)$$

In Eq. (2), $a_1$, $a_2$, $a_3$ represent contributions from the inner and outer elements for an odd-element array. For a single element $a_2 = a_3 = 0$, and for the-three element array $a_3 = 0$.

## 4. COMPARISON OF THEORY AND MEASURED RESULTS

The measured H-plane substrate-side angular power patterns are presented, along with the theoretical power patterns, for the following cases. Results for a dual-dipole array of fixed spacing, with a bolometer shifted to the far left, a centered bolometer, and a bolometer shifted to the far right are presented in Figures 2, 3, and 4. Results for the single-element, three- and five-element arrays are presented in Figures 5–7.

## 5. DISCUSSION

### *5.1 Dual-Dipole Beam Shifting*

For the case of the centered bolometer, the pattern is fairly symmetric about the broadside direction, showing off-axis peaks on both sides, and a slight null at broadside. The measured H-plane pattern is wider than is predicted. The main reason appears to be that as the device is rotated in the H-plane, illuminated lead lines begin to contribute to the response. We do not see a similar pattern-widening effect for E-plane measured data. The E-plane data is not included, since our present concern is phasing effects, which are seen only in the H-plane. For the case of the bolometer placed to the left and right, the patterns show that the main beam changes quadrants as expected. Differences in the measured side-lobe levels for the two cases may be caused by the asymmetry of the arrangement of the readout lines. An additional source of error that is not accounted for in the theoretical patterns is the finite size of the bolometer. The fact that it is a distributed load rather than a point load will give some range of phase additions when the current waves are summed at the load. Letting the loss per unit length of the CPS line vary near the nominal value does not improve agreement between theory and experiment.

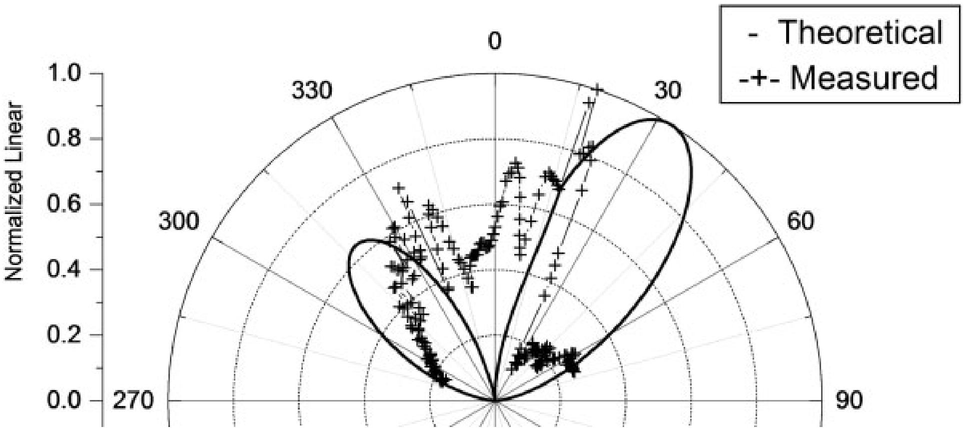

**Figure 4** H-plane substrate-side power pattern for dual-dipole antenna array with bolometer shifted to the left

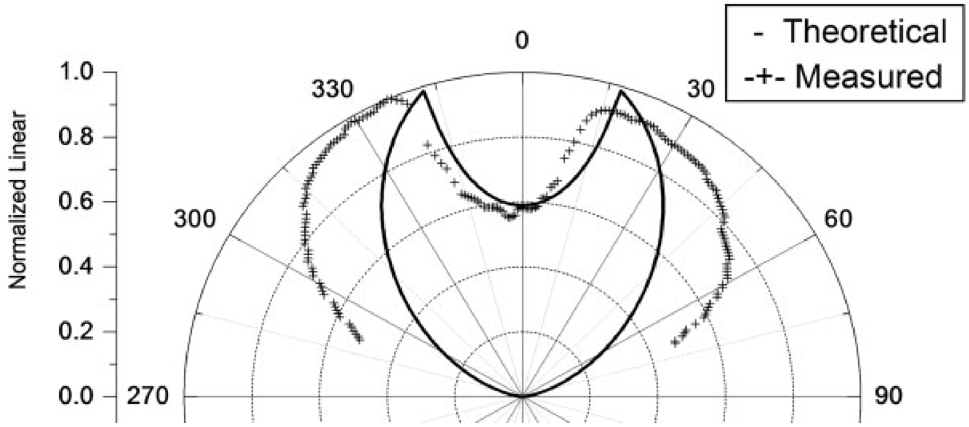

**Figure 5** H-plane substrate-side power pattern for a single element

*5.2 Beam Narrowing*

Considering the H-plane substrate-side patterns, there is a reduction in beam width in both the three- and five-element array, compared to the single-element case. There is somewhat more narrowing for the five-element case, as expected. The H-plane patterns are wider than expected, as discussed above. This feature is consistent, being seen in the data of Figures 5–7. The other sources of error discussed above also contribute. Again, varying the attenuation constant of the CPS lines does not significantly improve the agreement.

## 6. CONCLUSION

H-plane substrate-side angular-response measurements were presented and compared to theory, which verify phased-array antenna behavior at a wavelength of 10.6 $\mu$m in the infrared. Beam-shifting

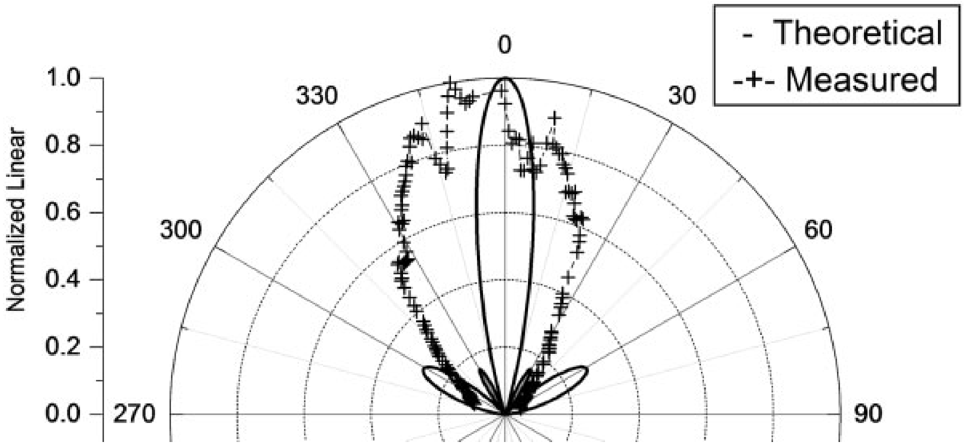

**Figure 6** H-plane substrate-side power pattern for a three-element array

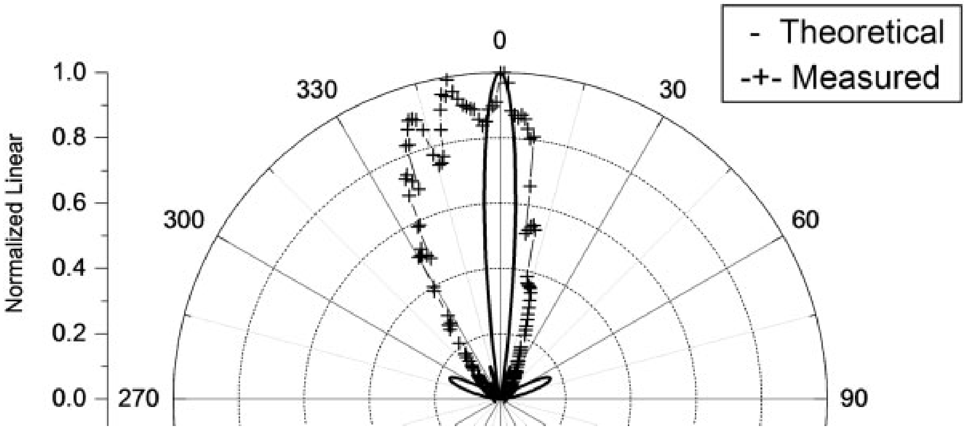

**Figure 7** H-plane substrate-side power pattern for a five-element array

and beam-narrowing behaviors were observed. Possible sources of error include the finite size of the bolometric load, as well as contributions from lead lines to the measured response.

## REFERENCES

1. C.T. Middlebrook, G. Zummo, and G.D. Boreman, Direct-write electron-beam lithography of an IR antenna-coupled microbolometer onto the surface of a hemispherical lens. J Vacuum Sci Technol B 24(2006), 2566–2569.
2. C.R. Brewitt-Taylor, D.J. Gunton, and H.D. Rees, Planar antennas on a dielectric surface. Electron Lett 17(1981), 729–731.
3. C.T. Middlebrook, B. Lail, and G.D. Boreman, Effect of a silicon immersion lens on the air-side and substrate-side response of infrared antenn-coupled bolometers. Submitted to IEEE Trans Antennas Propag.
4. T. Mandviwala, B. Lail, and G. Boreman, Infrared-frequency coplanar striplines: Design, fabrication, and measurements. Microwave Opt Technol Lett 47(2005), 17–20.
5. J.D. Kraus and R.J. Marhefka, Antennas for all applications, 3rd ed., New York: McGraw-Hill, 2002. xviii, 938 p.

---

# MULTIWAVELENGTH YB-DOPED FIBER RING LASER BASED ON A MACH-ZEHNDER INTERFEROMETER

**Chenghou Tu, Wengang Guo, Yongnan Li, Shuanggen Zhang, Hui Zhu, and Fuyun Lu**
Institute of Physics, Nankai University, Tianjin 300071, China; Corresponding author: lufy@nankai.edu.cn

*Received 26 July 2007*

**ABSTRACT:** *We proposed and demonstrated a room-temperature multiwavelength Yb-doped fiber ring laser with high stability based on a Mach-Zehnder interferometer by exploiting spatial hole burning and polarization hole burning effects, from which stable eight lasing wavelengths is obtained. The number of the lasing wavelengths (eight) is the most to our knowledge, and the wavelength spacing is 1.1 nm. Triple-, and dual-wavelength operation with the wavelength spacing of 1.1 nm or its integral multiples have been obtained by adjusting the intracavity polarization controllers.* © 2008 Wiley Periodicals, Inc. Microwave Opt Technol Lett 50: 723–725, 2008; Published online in Wiley InterScience (www.interscience.wiley.com). DOI 10.1002/mop.23206

**Key words:** *multiwavelength; Yb-doped fibe ring laser; Mach-Zehnder Interferometer(MZI); polarization hole burning effect(PHB)*

## 1. INTRODUCTION

In recent years, the research of multi-wavelength fiber laser attracts more attention because of its extensive applications in dense wavelength-devision mutiplexed (DWDM) communication systems, optical fiber sensors, optical instrument testing, spectroscopy, and so forth. Multiwavelength erbium fiber lasers have been demonstrated with various methods. The methods involve incorporating a high birefringence fiber loop mirror [1, 2] in the cavity, or using a highly nonlinear photonic crystal fiber and sampled bragg grating [3, 4], or adopting a delayed interferometer in the cavity [5]. Until now there are few reports about multiwavelength Yb-doped fiber. Feng et al. realized switchable dual wavelength Yb-doped fiber laser based on few mode fiber grating [6], and Chi et al. realized six wavelength Yb fiber laser using a multimode fiber based spatial-mode beating filter [7].The main obstacle to achieve multiwavelength operation at room temperature with a single piece of erbium-doped fiber (EDF) or ytterbium-doped fiber (YDF) is the homogeneous gain broadening [8], which induces strong mode competition and unstable laser output. Therefore to realize simultaneously stable lasing oscillation, the homogeneous broadening should be suppressed. To date, several methods have been proposed and successfully demonstrated. Such as using nitrogen cooling technique [9], exploiting polarization hole burning (PHB) effects [10, 11], etc.

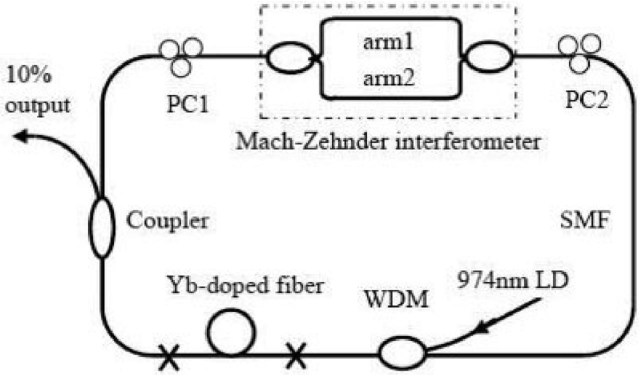

**Figure 1** Schematic diagram of the proposed laser

In this letter we demonstrated a stable 8 wavelength Yb-doped fiber ring laser based on a Mach-Zehnder interferometer(MZI) spectrum filter by exploiting PHB effects in the cavity, which has a simple structure and is low cost. By adjusting the position of polarization controller, dual- and triple-wavelength operation with the wavelength spacing of 1.1 nm to its integral multiples can be achieved.

## 2. EXPERIMENTAL SETUP AND THEORY

The fiber laser we proposed has a cavity configuration as illustrated in Figure 1. The cavity comprises a segment of 2.5 m ytterbium-doped fiber (the absorption at 975 nm is about 250 dB/m, the mode field diameter at 1060 nm is about 7.5 $\mu$m), a Mach-Zehnder interferometer made of two 50:50 fiber couplers, two fiber polarization controllers (PC) used to control the polarization state of the traveling light, a 974 nm pump LD and several segments of 1060 nm single mode fiber (SMF). The pump LD can supply up to 400 mw optical power. A 10:90 optical coupler is used as the output coupler, which couples 10% of the power out of the ring cavity. An optical spectrum analyzer (OSA, ANDO AQ6370) with a resolution of 0.02 nm is used to do all the measurements.

The multiwavelength laser operation is based on a MZI serving as the comb-like multichannel filter, which is the key element. The length of arm1($L_1$) is a little longer than that of arm2($L_2$), and the length difference $\Delta L = L_1 - L_2$. The optical intensity at the MZI output can be given by [5]:

$$I_{\text{out}}(\lambda) = I_{\text{arm1}}(\lambda) + I_{\text{arm2}}(\lambda) + 2\sqrt{I_{\text{arm1}}(\lambda) \cdot I_{\text{arm2}}(\lambda)} \cdot \cos(\Delta\phi) \quad (1)$$

and

$$\Delta\phi = \frac{2n\pi}{\lambda} \cdot \Delta L \quad (2)$$

where $n$ is the refractive index of fiber, $I_{\text{arm1}}$ and $I_{\text{arm2}}$ represent the optical intensity of arm1 and arm2, respectively. $\Delta\phi$ is the phase delay between the two arms because of the length difference $\Delta L$.